Helmholtz-Zentrum Dresden-Rossendorf (HZDR)

Sensitivity control of carbon nanotube based piezoresistive sensors by drain-induced barrier lowering

Böttger, S.; Wagner, C.; Lorkowski, F.; Hartmann, M.; Schuster, J.; Hermann, S.;

Originally published:

June 2019

Sensors and Actuators A 295(2019), 288-295

DOI: https://doi.org/10.1016/j.sna.2019.06.003

Perma-Link to Publication Repository of HZDR:

https://www.hzdr.de/publications/Publ-27781

Release of the secondary publication
on the basis of the German Copyright Law § 38 Section 4.

CC BY-NC-ND

Sensitivity control of carbon nanotube based piezoresistive sensors by drain-induced barrier lowering

Simon Böttger[1,*], Christian Wagner[1,3], Florian Lorkowski[2], Martin Hartmann[1], Jörg Schuster[4, 5], Sascha Hermann[1,4,5]

[1]*Center for Microtechnologies (ZfM), University of Technology Chemnitz, Chemnitz D-09111, Germany*

[2]*Institute of Physics, University of Technology Chemnitz, Chemnitz D-09111, Germany*

[3]*Helmholtz-Zentrum Dresden-Rossendorf (HZDR) ,Dresden D-01328, Germany*

[4]*Fraunhofer Institute for Electronic Nano Systems (ENAS), Chemnitz D-09126, Germany*

[5]*Center for Advancing Electronics Dresden (cfaed), Technical University Chemnitz, Chemnitz D-09111, Germany*

* Corresponding author

Simon Böttger

Center for Microtechnologies

Technische Universität Chemnitz

Straße der Nationen 62, 09111 Chemnitz, Germany

E-mail: simon.boettger@zfm.tu-chemnitz.de

Tel: 0049 371 531 32374

Fax 0049 371 531 8 32374

Christian Wagner / E-mail: c.wagner@hzdr.de

Florian Lorkowski / E-mail: florian.lorkowski@s2015.tu-chemnitz.de

Jörg Schuster / E-mail: joerg.schuster@enas.fraunhofer.de

Martin Hartmann / E-mail: martin.hartmann@zfm.tu-chemnitz.de

Sascha Hermann / E-mail: sascha.hermann@zfm.tu-chemnitz.de

Keywords: carbon nanotube, CNT-FET, piezoresistive sensor, piezoresistive effect, DIBL, transport modelling

Abstract

The superior performance of membrane-based carbon nanotube (CNT) sensors showing maximum gauge factors of up to 800 is analyzed by a device study combining technological and theoretical approaches. Drain-induced barrier lowering (DIBL) is found to contribute significantly to this high sensitivity. A high subthreshold voltage roll-off of $(750 \pm 200)\,\mathrm{mV} \cdot \mathrm{V}^{-1}$ and degradation of subthreshold swing is observed even for channel length of $200\,\mathrm{nm}$. The piezoresistive behavior of the CNT sensor running in the DIBL regime is shown as a complex and input-voltage dependent interplay of strain-dependent Fowler-Nordheim tunneling and the intrinsic thermionic resistance change. We show, that this interplay can be controlled by the applied bias voltages V_{GS} and V_{DS} in such a way, that the overall sensitivity is enhanced up to $150\,\%$ with respect to the intrinsic effect. The control of the sensitivity via V_{DS} is enabled by the DIBL effect, which appears for our CNT device at remarkably long CNT-channels.

The experimental findings are retraced by a simplified transport model, which combines a numerical device solver with an electronic model for strained carbon nanotube based field-effect transistors (CNT-FETs) covering thermionic as well as tunneling contributions. Strain dependent tunneling through the Schottky barriers (SBs) appears to be the key contribution to the strain sensitivity in our model. From the model device characteristics have been derived which reproduce the experimental findings emphasizing the significance of tunneling processes in combination with DIBL effects for the superior strain sensitivity of our device.

1. Introduction

Scalable fabrication of electronics and sensors requires new and innovative approaches in the context of Industry 4.0, the Internet of Things and flexible electronics. One of these approaches is using functional nanomaterials like single-walled carbon nanotubes (SWCNTs). The intrinsic properties of SWCNTs, such as a high young's modulus up to 1 TPa [1, 2], mechanical strength up to 52 GPa [3] and a giant intrinsic piezoresistivity [4–7] facilitate a new class of miniaturized strain sensors standing out by versatile integration capabilities on different substrates or in complex systems.

There is still a lack of industrial-suited integration methods, although first prototype devices have been fabricated more than one decade ago by means of search and contact technology [6–9] or tedious pick-and-place methods [10]. The reproducible fabrication of those devices demands extremely efficient CNT separation routines, since the magnitude of the intrinsic piezoresistive effect is strongly correlated to the CNT structure, e.g. diameter and chiral angle [11]. For liquid CNT dispersions, huge progress was made for pre-separation of CNTs according to CNT-length [12–14], electronic type [15–17] and chirality [18] up to the mono-chiral level. Additionally, the control of the assembly structure and alignment of CNTs towards the strain direction for piezoresistive devices is mandatory. Hence, dielectrophoresis is a highly-suited integration technique here, since it facilitates precise control of the CNT alignment and amount [12, 19, 20].

Up to now, the piezoresistive effect in carbon nanotubes was intensively studied at low drain-source voltages, where parasitic short-channel effects like drain-induced barrier lowering (DIBL) do not play a significant role. The DIBL effect is well-known in the front-end-of-line as it adversely affects the metal-oxide-semiconductor field-effect transistor (MOSFET) performance. By scaling

down their size, the figure of merit such as subthreshold swing SS and off current I_{off} degrade due to increased source-drain current leakage [21–23]. Although theoretically predicted for carbon nanotube-based field-effect transistors (CNT-FETs) [24, 25], the existence of a significant DIBL was not experimentally investigated up to now [26]. A parametric investigation of the piezoresistive effect of a CNT-FET operating in the DIBL regime will gain better understanding of the piezoresistive effect and the underlying fundamental mechanisms in SWCNT devices.

2. Materials and Methods

2.1. Sensor fabrication

The fabrication of the piezoresistive sensors was carried out with particular care in order to achieve systematical and parametric studies at well-defined strain states. Therefore CNTs were integrated at strained sites near the edge of a MEMS membrane as schematically shown in figure 1a. This configuration was chosen since membrane based MEMS pressure sensors can easily be actuated by applying differential pressure without changing the electrostatic environment of the sensor significantly. Thus parasitic effects on electrical transport measurements can be excluded.

The wafer-level manufacturing process chain is based on $150\ \mathrm{mm}$ silicon-on-insulator substrate wafers having a device layer of $d = (5.0 \pm 0.5)\ \mu\mathrm{m}$, defining the membrane thickness. The complete technology process flow is similar to what we published previously [27]. In short, an anisotropic deep reactive ion etching step, followed by wet etching of the residual oxide on the wafer backside is used to define membranes at allocated positions. Afterwards, the wafer is covered by a SiO_2 $(10\ \mathrm{nm})$ / Si_3N_4 $(100\ \mathrm{nm})$ high-k dielectric layer stack formed by thermal

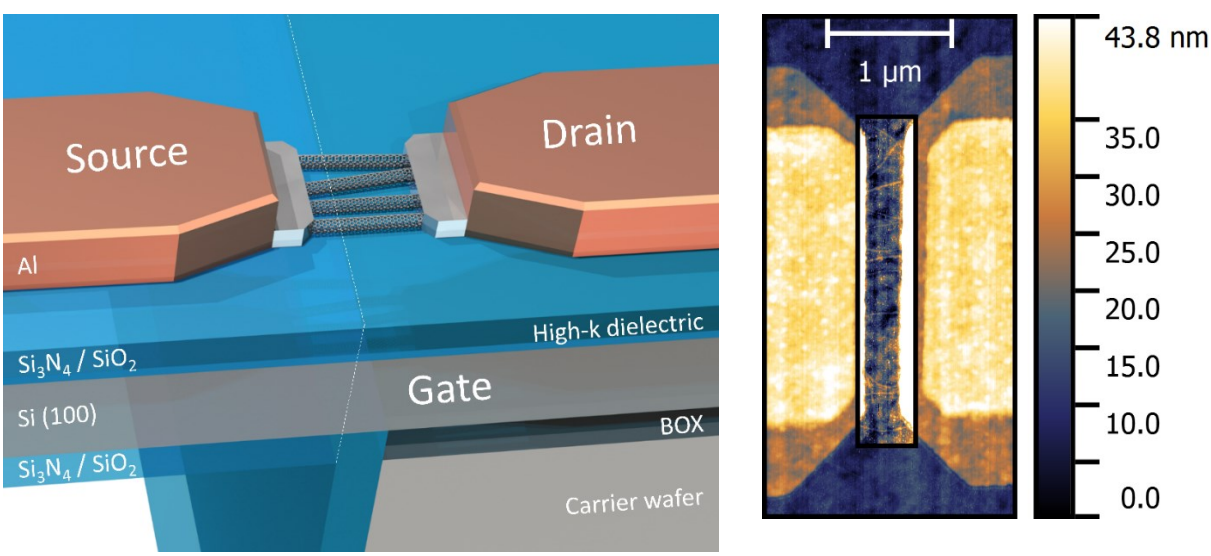

a b

Figure 1: Schematic of the fabricated sensor structures (a) and an AFM image of the channel area of one representative device (channel does not fit to color scale).

oxidation and a dichlorosilane / ammonia based low-pressure chemical-vapor deposition, respectively. Subsequently, assembly electrodes are formed by electron beam lithography (EBL) on a PMMA based dual-resist system followed by physical vapor deposition (PVD) of $5\ \mathrm{nm}$ Ni and $15\ \mathrm{nm}$ Pd, and an acetone based lift-off process. Furthermore, an additional lithography / PVD / lift-off sequence was conducted, in order to form Al ($200\ \mathrm{nm}$) / Pd ($10\ \mathrm{nm}$) sensor periphery and interconnects. Afterwards, CNTs (IsoNanotubes-S™, NanoIntegris [28]) were integrated via a sequentially driven dielectrophoresis deposition process. The corresponding processing tool was scaled up to be able to perform automated wafer-level processes featuring high control over CNT assembly in terms of site-selectivity, alignment, density, purity as well as throughput. For the deposition process, an AC signal with a frequency of $f = 10\ \mathrm{MHz}$ and a coupling voltage amplitude of $V = 2.9\ \mathrm{V}$ was applied. Afterwards, the sample was intensively rinsed with deionized water and annealed at $200\ ^\circ\mathrm{C}$ in ambient air. Subsequently, the CNT ends were fully embedded and top contacted by additional EBL / PVD / lift-off process steps forming a channel length of $200\ \mathrm{nm}$. Finally, the samples were vacuum-annealed at $p < 5 \cdot 10^{-3}\ \mathrm{Pa}$ at $300\ ^\circ\mathrm{C}$ in order to improve the electromechanical contacts.

2.2 Electrical Characterization

The sensor was electrically characterized in nitrogen atmosphere at a temperature of $22\ ^\circ\mathrm{C}$ in order to reduce influence from ambient conditions, such as electrostatic doping from water and air [29]. In order to facilitate membrane actuation and electrical characterization of the CNT-FET at the same time, a special characterization set-up was arranged which avoids actuation induced measurement artifacts. Before measurement the sample was annealed at $200\ ^\circ\mathrm{C}$ inside the glovebox for two hours in order to desorb residual oxygen and water molecules. Afterwards, the

CNT-FET was electrically characterized with a Keithley SourceMeter® 2636b at different drain-source- and gate-source voltages ($V_{\mathrm{DS}}, V_{\mathrm{GS}}$). In order to suppress hysteresis effects in the transfer characteristics, measurements were performed in reversed-pulse mode (see supplementary data). The CNT-FET drain current was recorded under variation of V_{DS} and V_{GS} and cyclic pressure actuation up to $p = 950\,\mathrm{mbar}$ differential pressure. Subsequently, characteristic sensor properties were extracted from those time traces by a scripted evaluation program. The extracted sensor properties are the relative change of the resistance $\Delta R \cdot R^{-1} = (R_0 - R_\varepsilon) \cdot R_0^{-1}$, the gauge factor $\beta_{\mathrm{GF}} = \Delta R \cdot R^{-1} \cdot \varepsilon^{-1}$, and the signal-to-noise ratio for current amplitudes $SNR = 20 \cdot \lg(\Delta I(\varepsilon) \cdot \sigma(I_0)^{-1})$, where R_0 is the device resistance upon no external strain, R_ε is the device resistance upon a strain of ε, ΔI is the strain-induced drain current change and σ is the standard deviation of the measured drain currents at no external strain I_0.

2.3. Transport modelling

In order to model the electronic conductance of the device, a one-dimensional ballistic CNT-FET device solver is implemented in order to obtain the gradient of the electrostatic potential ϕ at the contact. This corresponds to the built-in electrical field $F = \mathrm{d}\phi \cdot \mathrm{d}x^{-1}$ and is equal to the slope of the conduction- and valence bands at the contacts. Due to symmetry constraints, this device model uses a wrap-around gate instead of a planar back-gate. However, the geometry is chosen in a way such that the gate capacitance is equivalent to the measured devices. Thus the results of the solver can be compared to the experimental data.

The charge current through the device is calculated by thermionic emission and tunneling through an approximately triangular barrier at the contact, which is schematically shown in figure 2a together with an equivalent circuit diagram of the CNT / metal junction. The Schottky barriers

formed at the source and drain junctions strongly affect the thermionic as well as the tunneling conduction for electron and hole transport [30–34]. The total conductance G_{tot} reads accordingly

$$G_{\mathrm{tot}} \approx 2G_0\left(e^{-\Phi_{\mathrm{VB}}/E_{\mathrm{th}}} + e^{-\Phi_{\mathrm{CB}}/E_{\mathrm{th}}} + |T|^2\right) = G_{\mathrm{th}} + 2G_0|T|^2. \qquad (1)$$

Here, G_0 denotes the CNT's quantum conductance and G_{th} the thermionic part of the total conductance while $|T|^2$ denotes the tunneling probability. Φ_{VB} and Φ_{CB} are the SB height of the valence band (VB) and conduction band (CB), respectively.

The tunneling probability $|T|^2$ through the barrier can be calculated using the Wentzel–Kramers–Brillouin (WKB) approximation, called Fowler-Nordheim tunneling [35]:

$$|T|^2 \approx \exp\left(-\frac{4\sqrt{2m^*}}{3\hbar eF}\Phi^{\frac{3}{2}}\right). \qquad (2)$$

Here, E_{th} denotes the thermal energy $E_{\mathrm{th}} = k_B T$, m^* the effective mass of the carriers, F the built-in electric field, which is strongly affected by the applied drain-source potential V_{DS}. A two-band model is applied with the valence band and the conduction band. When mechanical strain is induced in such a device, the piezoresistive effect changes the bandgap and thus modifies the SBs at the source and drain junctions. This strain dependence of the SB is given by [11, 36–38]:

$$\Phi(\varepsilon) = \Phi_0 + \frac{\gamma}{2}\varepsilon, \text{ whith } \gamma = 3t_0(1+\nu_{\mathrm{CNT}})\cos(3\theta_{\mathrm{CNT}}), \qquad (3)$$

such that $\gamma_{\max} = 3.6t_0 \approx 9.4$ eV. Here, Φ_0 is the SB height in the unstrained state, $t_0 = 2.66$ eV the tight-binding parameter of Graphene, $\nu_{\mathrm{CNT}} \approx 0.2$ the CNT Poisson's ratio [37, 39–41] and θ_{CNT} the chiral angle of the CNT. Further, within the framework of the tight-binding model the CNT effective mass shows the same strain-dependence as the band gap [11, 37, 41].

3. Results and discussion

3.1. Simulation of strain-dependent device characteristics

Equation 1 indicates that both transport modes – thermionic and tunneling transport – show a different dependence on the Schottky barrier height Φ. Hence, both transport modes will contribute differently to the strain-induced change of the conductance. In contrast to thermionic transport, the tunneling current is affected by the built-in electric field F according to equation 2. The overall (differential) gauge factor can be calculated using equations 1 and 2 including the change of the gap and effective mass with strain (see also supplementary data):

$$\beta_{\mathrm{GF}} = \frac{1}{R}\frac{dR}{d\varepsilon} = -\frac{1}{G_{\mathrm{tot}}}\frac{dG_{\mathrm{tot}}}{d\varepsilon} = -\left(\frac{G_{\mathrm{th}}}{G_{\mathrm{tot}}^2}\frac{dG_{\mathrm{th}}}{d\Phi}\frac{\partial\Phi}{\partial\varepsilon} + \frac{2G_0|T|^2}{G_{\mathrm{tot}}^2}\left(\frac{\partial|T|^2}{\partial\Phi}\frac{\partial\Phi}{\partial\varepsilon} + \frac{\partial|T|^2}{\partial m^*}\frac{\partial m^*}{\partial\varepsilon}\right)\right). \quad (4)$$

The contribution of the thermionic and tunneling on the gauge factor is depicted in figure 2c. The thermionic current (dashed lines) is independent of the SB width and built-in electrical field F and thus yields a constant conductance change upon the built-in electric field, for a certain amount of induced strain. At a low electric field, the thermionic effect dominates the overall sensor performance with a moderate gauge factor per band of $\beta_{\mathrm{GF}} \approx 170$. This value corresponds to half of the gauge factor one would expect from the strain-dependence of the band gap using the Yang-Han equation [36] for $\theta_{\mathrm{CNT}} = 0°$ (about 340 in the linear strain regime). Strain – in theory – leaves the Fermi level of the CNT unaltered, which means that strain shifts the conduction and the valence band equally towards opposite directions. Thus, the shift of the SB for each band is half the shift of the band gap.

The tunneling current, in contrast, is strongly affected by the built-in electrical field F. Upon increasing F the tunneling probability becomes larger (sharper triangle), as the effective SB width reduces, until the tunneling current dominates the overall device conductance (see figure 2b).

The strain dependence of this tunneling current is a function of the built-in electrical field (see SI). These dependencies lead to the characteristic behavior of the overall device sensitivity (gauge factor) shown as solid lines in figure 2c upon the built-in electric field F. In order to maximize the sensor sensitivity, a moderate built-in electric field F is required, which depends on the magnitude of the SB according to Schottky-Mott rule. Since the built-in electric field F is tuned by the bias voltages V_{DS} and V_{GS}, the sensitivity is expected to strongly change with those bias voltages.

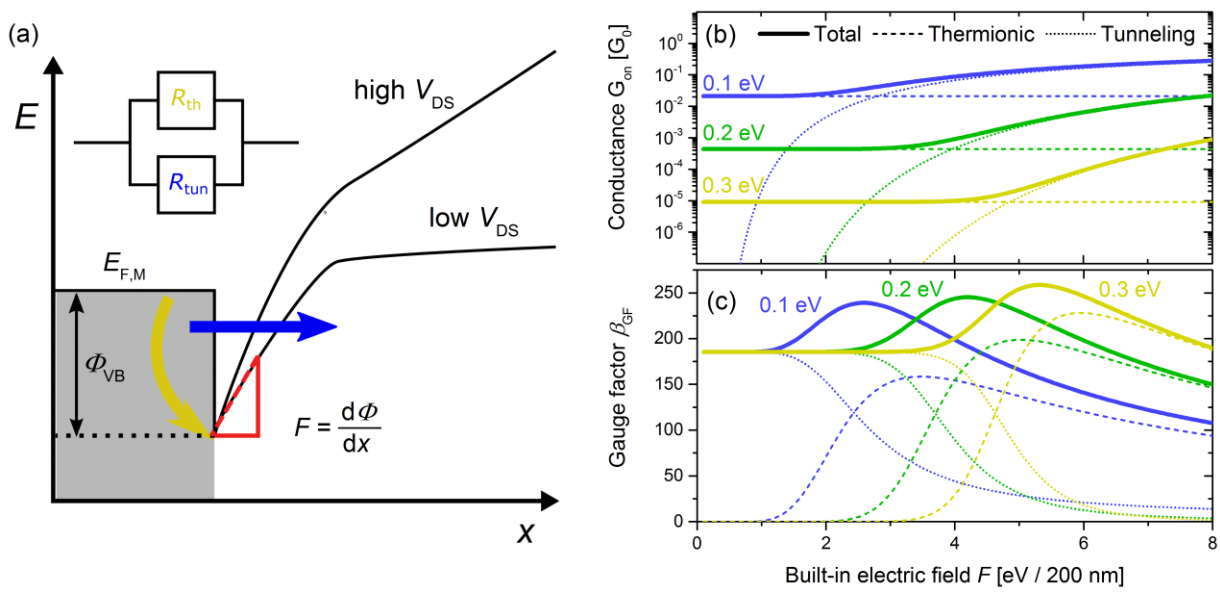

Figure 2: (a) Sketch of the metal-semiconductor junction model at the contacts together with the equivalent circuit diagram. Specifically, the valence band bending and the Schottky barrier formation for holes at the source contact is shown. (b) Contribution from thermionic and tunneling currents to total device conductance for different V_{DS}. (c) Simulated differential gauge factor of a CNT device with Schottky contacts for different electric fields (potential gradients) and Schottky barriers. The contributions from thermionic (dotted line) and tunneling (dashed line) charge carrier transport are weighted with respect to the total current of the system (for more information see supplementary data). The electrostatic potential gradient is related to the device channel length of 200 nm.

3.2. Drain induced barrier lowering and its influence on the sensor sensitivity

First, the electrical characteristics of the CNT-FET are measured to capture the full working range of the device. Figure 3a shows the transfer characteristics of the CNT-FET for a drain-source voltage range from $-2.5\ \mathrm{V} \leq V_{\mathrm{DS}} \leq -0.5\ \mathrm{V}$.

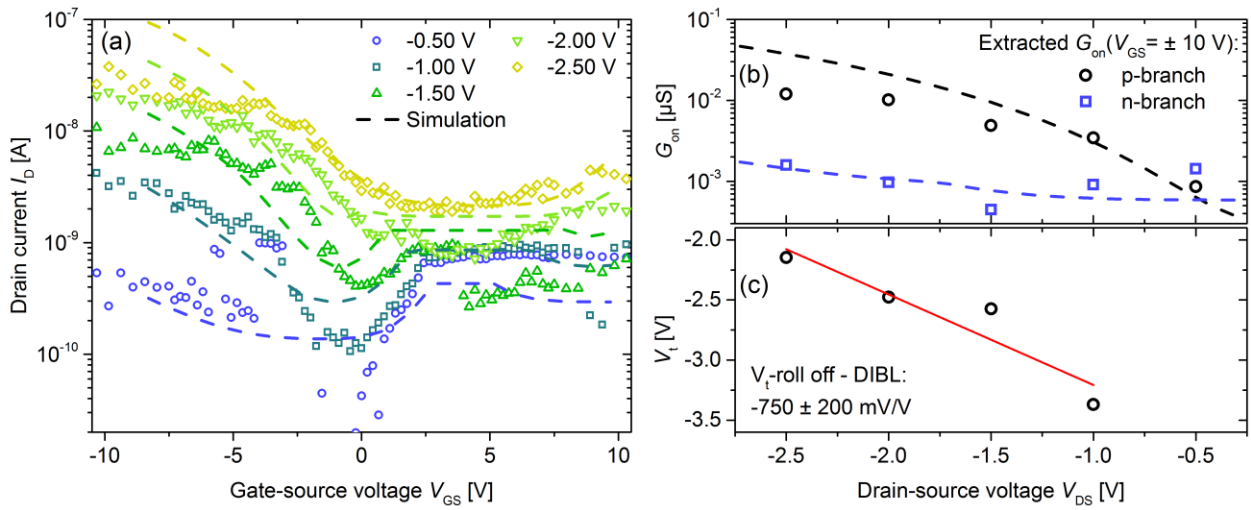

Figure 3: (a) Transfer characteristics at different V_{DS} and corresponding curves from transport simulations (dashed lines) with $E_{\mathrm{gap}} = 0.52\ \mathrm{eV}$, $\Phi_{\mathrm{VB}} = 0.27\ \mathrm{eV}$ and $\Phi_{\mathrm{CB}} = 0.27\ \mathrm{eV}$. (b) On-conductance for holes and electrons as the majority charge carriers in the p-branch and n-branch, respectively. Values are extracted from experimental and modelled (dashed lines) transfer characteristics at $V_{\mathrm{GS}} = \pm 10\ \mathrm{V}$. (c) Subthreshold voltage V_{t} and linearly fitted V_{t} roll-off from experimental data.

The CNT-FET shows an ambipolar behavior for low drain-source voltages V_{DS}, characterized by nearly symmetrical formed p- and n-branches, which are clearly separated by a current minimum at around zero gate-source voltage. In the on-state regime ($|V_{\mathrm{GS}}| > 5\ \mathrm{V}$) the p- and n-currents are approximately of the same magnitude. This indicates a nearly symmetric band alignment with respect to the Fermi energy of the contact metal $E_{\mathrm{F,M}}$ and hence, similar Schottky barriers for the p- and n-branch are expected. Increasing $-V_{\mathrm{DS}}$ significantly changes the transfer characteristics

from ambipolar to p-type like behavior with vanishing off regime, mainly characterized by two distinct trends: First, the p-branch subthreshold voltage $V_{t,p}$ shifts towards positive gate-source voltage V_{GS} and second, the asymmetric behavior of the on-conductance G_{on} for p and n dominated transport. The latter is extracted from transfer curves at $V_{\mathrm{GS}} = \pm 10\ V$ and is shown in Figure 3b. This figure depicts that $G_{\mathrm{on},p}$ rises significantly upon increasing $-\mathrm{V}_{\mathrm{DS}}$, whereas $G_{\mathrm{on},n}$ remains nearly constant. This leads to an asymmetry of almost one decade. Both effects indicate a short-channel effect called DIBL, where the CNT-FET band deformation does not only happen through V_{GS} but rather through superimposed electric fields due to the large drain potential. To fully understand the underlying mechanism and for an accurate determination of the SB, electrical transport simulations as introduced in section 2 have been conducted.

Figure 3 further shows the result of the transport simulations, which are in concordance to the measured transfer curves. The transport model is based on CNTs with a bandgap of $E_{\mathrm{gap}} = 0.52\ \mathrm{eV}$, Schottky barriers of $\Phi_{\mathrm{VB}} = 0.27\ \mathrm{eV}$ and $\Phi_{\mathrm{CB}} = 0.25\ \mathrm{eV}$, and $m^{*} = 0.6\ \mathrm{m_{el}}$, which fits well to the integrated CNTs having diameters between $1.2\ \mathrm{nm}$ and $1.7\ \mathrm{nm}$ [42, 43]. The increase of $G_{\mathrm{on},p}$ can be related to the large dependence of the SB width on V_{DS} at the source junction. The source barrier is the dominating barrier for the hole transport in the p-branch regime since most of the drain potential is dropped at the source junction, leading to a comparatively higher built-in electric field at this SB [34] (see also supplementary data). Hence, the tunneling probability raises significantly upon increasing $-V_{\mathrm{DS}}$, which leads to an additional contribution to the overall conductance and consequences in an increase of $G_{\mathrm{on},p}$. The remaining deviations of $G_{\mathrm{on},p}$ between experiment and simulations for drain-source voltages above $1.0\ \mathrm{V}$ are presumably related to the necessary simplifications during modeling. Moreover we expect a

certain chirality mix of the integrated CNT assembly, which results in heterogeneous electronic properties of the CNTs (e.g. band gap) and thus influence the transfer curves. For the n-branch, the dependence of the on-conductance on V_{DS} is much less pronounced which is due to a lower built-in electric field F at the drain junction for negative V_{DS}.

The electrical transfer curves indicate on a degradation of the gate controllability, since the subthreshold swing SS significantly increases with V_{DS} as shown in table 1. Moreover, a systematic shift of the transfer curves towards positive V_{GS} upon applied V_{DS} can be detected, which is known as the subthreshold voltage roll-off (V_{t} roll-off). These two observations are typical indications on the existence of DIBL [21, 23, 24]. From the extracted subthreshold voltages shown in figure 3b, the V_{t} roll-off is determined by a linear fit to $(-750 \pm 200)\ \mathrm{mV} \cdot \mathrm{V}^{-1}$, which is significantly higher than in advanced MOSFETs. To our knowledge, this is the first time such a high DIBL is experimentally observed in CNT-FETs at relatively large channel length of $200\ \mathrm{nm}$. A significant DIBL is mainly reported for sub $10\ \mathrm{nm}$ devices, e.g. by Qiu *et al.* [44] who observed a significant degradation of subthreshold swing and off-current. We explain the high DIBL in our devices by the low gate capacitance caused by the $110\ \mathrm{nm}$ thick gate dielectric on a global Si back-gate and the comparatively high V_{DS}.

Table 1: CNT-FET properties upon applied V_{DS}

V_{DS} [V]	-0.5	-1.0	-1.5	-2.0	-2.5
$G_{\mathrm{on},p}$ [nS]	0.9	3.4	4.9	10.1	10.2
$G_{\mathrm{on},n}$ [nS]	1.4	0.9	0.5	1.0	1.2
V_{t} [V]	–	-3.4	-2.6	-2.5	-2.1
SS [V/dec]	1.28 ± 0.17	2.20 ± 0.31	2.35 ± 0.19	3.60 ± 0.13	3.84 ± 0.21

The DIBL effect is expected to influence the sensitivity of the CNT sensor, as the piezoresistive effect not only influence the thermionic transport through the CNTs, it also modifies the SBs through strain-induced bandgap changes. Moreover, a significant dependence of the sensitivity on V_{DS} is expected, since built-in electric fields are modified by V_{DS} as described earlier. In order to elaborate these expectations and to determine the optimal sensor operation point, a parametric study for the bias voltages V_{DS} and V_{GS} was conducted. Therefore, the sensor response was captured for 25 different pairs of V_{DS} and V_{GS}. Figure 4a shows such a typical response curve with two clearly separated current levels, each depicting a Gaussian current distribution. The gauge factor β_{GF} is calculated from these characteristics. The induced strain ε is assessed from a calibrated finite element model of the corresponding device (see supplementary data and [45]). Figure 4b shows an interpolated contour plot of the experimentally determined gauge factor

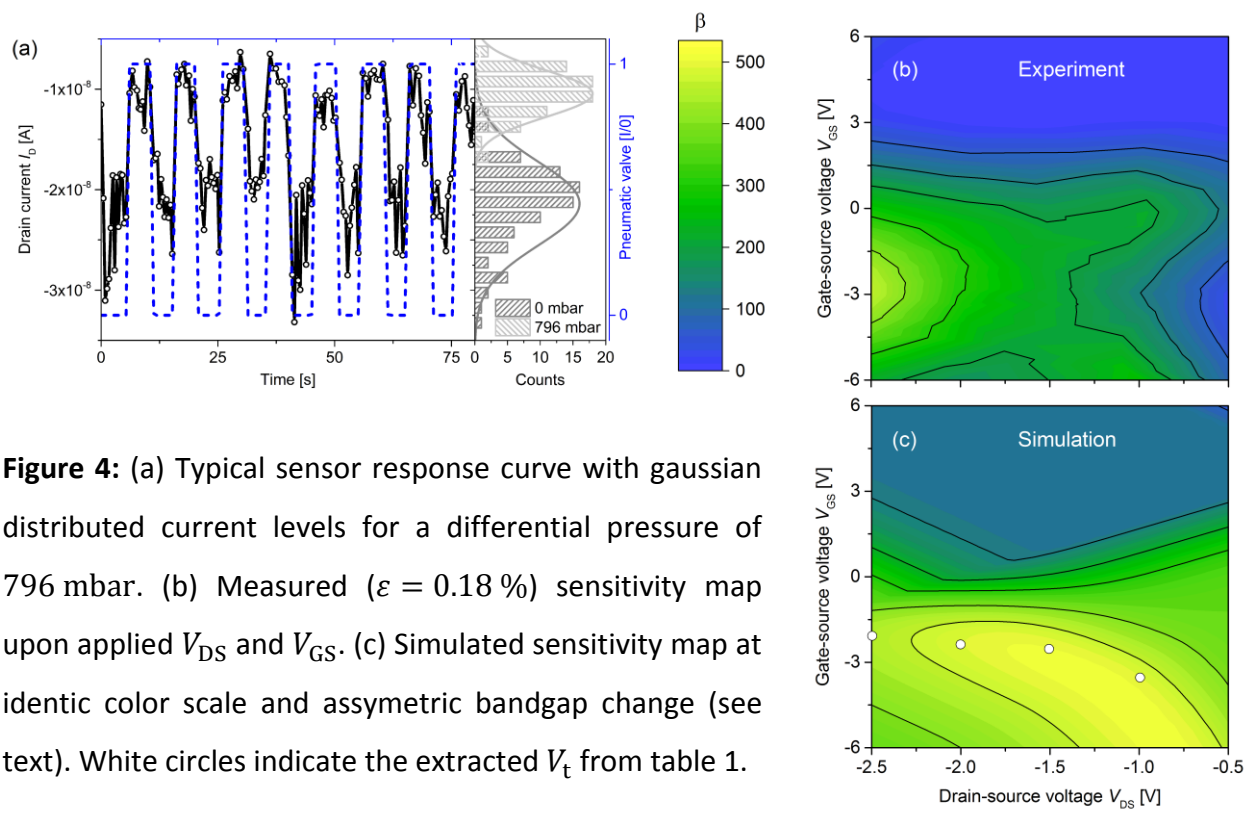

Figure 4: (a) Typical sensor response curve with gaussian distributed current levels for a differential pressure of $796\ \mathrm{mbar}$. (b) Measured ($\varepsilon = 0.18\ \%$) sensitivity map upon applied V_{DS} and V_{GS}. (c) Simulated sensitivity map at identic color scale and assymetric bandgap change (see text). White circles indicate the extracted V_{t} from table 1.

(color-coded) depicting an inhomogeneous sensitivity distribution in the measured parameter range ($-2.5\ \mathrm{V} \leq V_{\mathrm{DS}} \leq -0.5\ \mathrm{V},\ -6.0\ \mathrm{V} \leq V_{\mathrm{GS}} \leq 6.0\ \mathrm{V}$).

In the n-branch ($V_{\mathrm{GS}} > 2.0\ \mathrm{V}$) as well as for low drain-source voltages $V_{\mathrm{DS}} > -1.0\ \mathrm{V}$ almost no sensor response can be observed, whereas the gauge factor is up to $\beta_{\mathrm{GF}} = 480$ at $V_{\mathrm{DS}} = -2.5\ \mathrm{V}$ and $V_{GS} = -3.0\ \mathrm{V}$. This is compared to the strain dependence of the earlier introduced transport model in order to understand the observed phenomena. Therefore the model was adapted by an asymmetrical strain-induced bandgap change whereby the bandgap opening is accounted to the valence band as described in the supplemental material. This assumption was first discussed by Helbling *et al.* [8] since a mismatch between the theoretical prediction and the experimentally observed gauge factor was found. It was stated that such asymmetric bandgap shift yields the highest strain-sensitivity in the subthreshold regime rather than in the off-state, which we also observed for our device. However, the specific mechanism is still unclear. As a hypothesis we relate this effect to a pinning of the CB, such that the Schottky-Mott rule is not applicable anymore. These pinning effects may occur due to a high amount of surface states of the Si_3N_4 dielectric as underlined by complete suppression of sensor response in the n-branch.

The simulated device sensitivity map shown in figure 4c is generally in a qualitative agreement to the experimentally observed result. The deviations between measurement and simulation at low V_{DS}, where – in contrast to experiment – large gauge factors are observed, are most probably due to measuring artefacts of the comparatively low drain currents there.

The shift of the sensitivity maximum towards positive V_{GS} upon increased $-V_{\mathrm{DS}}$ is another characteristic trend, which is more pronounced in the simulated sensitivity map. The magnitude of that shift is similar to the V_{t} roll-off, as shown by the white circles in figure 4c. This implies that

the inhomogeneous behavior of the CNT sensor sensitivity can obviously be related to the DIBL effect. As discussed earlier, the DIBL effect is mainly affected by the bandgap and the magnitude of the Schottky barriers as well as by the built-in electric field F. Although the role of the contacts in CNT based piezoresistive sensors was previously unclear and some strain dependence was expected [6, 7, 10, 36] it has always been attempted to minimize or to prevent Schottky barrier formation in such CNT sensors in order to observe the intrinsic effects [5, 8, 9]. Within this work the crucial role of SBs on the sensor sensitivity could be shown. Moreover an increase in sensitivity, with respect to the maximal intrinsic thermionic gauge factor ($\beta_{GF,th} = 340$) of more than 50% to a total gauge factor of $\beta_{GF,tot} = 510$ could be achieved for this specific device. This significant increase can be explained by the high sensitivity of tunneling currents on strain-induced modulations of the SB.

These findings lead us to conclude with a further developed guideline for configuration and operation of those sensors: Firstly, the work function of contact metals and the CNTs bandgap predominantly determine the SBs and hence defines the operation point. As the degree of freedom is low with regard to the choice of material, we rather suggest to control the sensor operation point by manipulating the built-in electric field F via the device geometry (channel length) and the applied drain-source voltage V_{DS}. Moreover, the CNT-FET threshold voltage position can be controlled and tuned by a price control of the dielectric environment of the CNTs. This can be done either via passivation approaches [46–48] or by choosing proper ambient conditions [29, 49, 50] . Utilizing these approaches the adjustment of the sensor operating point for forthcoming sensor generations can be realized to $V_{\mathrm{GS}} = 0\ \mathrm{V}$, which gains reduced complexity and fabrication costs, since the gate electrode becomes redundant.

3.3. Intrinsic sensor properties at the sensor operation point

To find out the operation point and maximum gauge factor of the specific sensor an in-depth study with comparatively higher data point density at a drain-source voltage of $V_{\mathrm{DS}} = -2.5\ \mathrm{V}$ was conducted and illustrated in figure 5. The extracted gauge factor (blue) at $\varepsilon = 0.18\ \%$ is provided together with the corresponding transfer curve. The sensitivity is a function of V_{GS} as described earlier. At the p-branch, the sensor shows a moderate gauge factor of β_{GF}~250. Close to the working point at $V_{\mathrm{GS}} = -2.5\ \mathrm{V}$ the sensitivity is significantly increased up to a maximum gauge factor of $\beta_{\mathrm{GF}}(\varepsilon = 0.18\ \%) = (600 \pm 160)$ and vanishes completely by further increasing V_{GS} above 2.5 V. Again a suppression of the sensitivity in the CNT-FET's n-branch is depicted, which is contrary to most previous studies on CNT based piezoresistive devices, where the highest gauge factors were observed in the off state [5, 7, 8, 51].

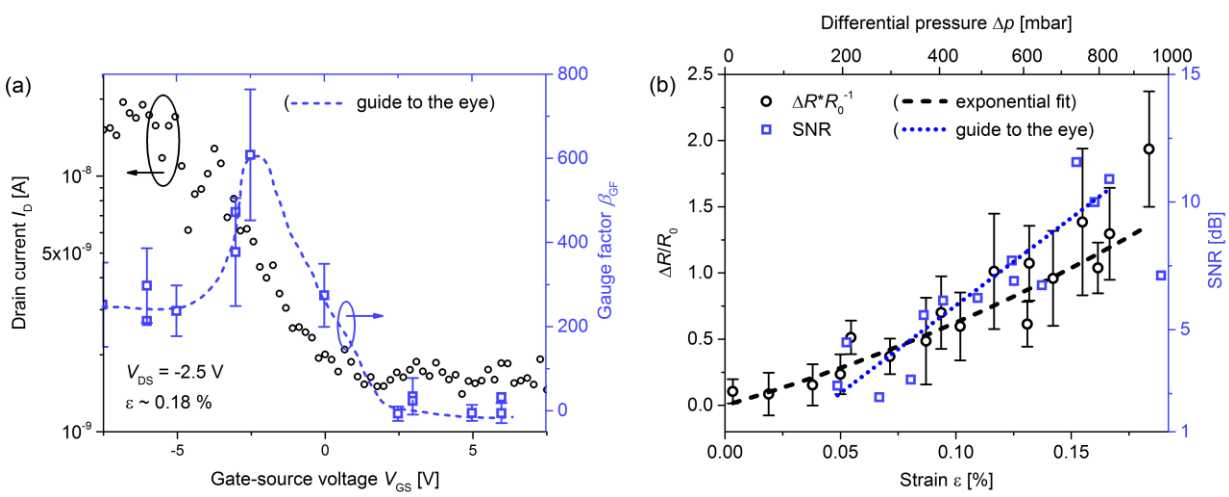

Figure 5: (a) The gauge factor as a function of the gate-source voltage V_{GS} at $V_{\mathrm{DS}} = -2.5\ \mathrm{V}$ and the corresponding transfer curve at induced strain of $\varepsilon = 0.18\ \%$. (b) Strain dependence of the relative resistance change and signal-to-noise ratio SNR at $V_{\mathrm{DS}} = -2.5\ \mathrm{V}$ and $V_{\mathrm{GS}} = -2.5\ \mathrm{V}$.

In order to assess the minimal detectable differential pressure Δp and the corresponding induced strain ε, the sensor was characterized at different applied Δp. The relative resistance change $\Delta R \cdot R^{-1}$ for each differential pressure was extracted in the same way as introduced earlier and plotted against Δp and ε in figure 5b. The relative resistance change increases up to around 150% ($\varepsilon \sim 0.20\ \%$) with strain. The data points tends to follow a $A \cdot \varepsilon \cdot e^{B \cdot \varepsilon}$ behaviour, indicated by the dashed line. Hence, there is an exponential strain dependence of the gauge factor $\beta_{\mathrm{GF}}(\varepsilon)$, as already predicted and observed in previous publications [4–6, 52]. The maximal observed gauge factor is up to $\beta_{\mathrm{GF}} = 800$ for an induced strain of $\varepsilon \sim 0.20\ \%$, that is close to the maximal observed gauge factors for membrane based CNT sensors (β_{GF} up to 850 [5, 7–9]). The signal-to-noise ratio SNR extracted from signal amplitudes increases linearly upon induced strain with a maximal SNR of $12\mathrm{dB}$ for $\varepsilon \sim 0.20\ \%$. With a suitable CNT passivation layer in forthcoming sensor generations the SNR is assumed to increase.

Conclusion

The joint experimental and simulation results of a strained CNT-FET show that the DIBL-effect is present even in $200\ \mathrm{nm}$ long CNT FET channels. This device-specific effect enhances the intrinsic strain-sensitivity of a wafer-level fabricated CNT sensor to a maximum measured gauge factor of $\beta_{GF} = 800$.

The experimental transfer characteristics and the gauge factor at comparably high drain-source voltages could be described by a simplified transport model including thermionic transport and Fowler-Nordheim tunnelling through a Schottky-barrier. Thereby the strain dependence of both transport modes gains deep insights into the fundamental mechanism at the Schottky barrier.

The studies suggest that the DIBL effect can be used to adjust the sensor operation point via the applied V_{DS} and the built-in electric field F and to push sensitivity. For the investigated device a sensitivity enhancement of $150\ \%$ could be demonstrated. Moreover an innovative approach for reducing complexity in forthcoming sensor generations, where gate electrode become redundant is proposed.

Acknowledgments

This work was partly financed by the Volkswagen Foundation within the initiative 'Integration of Molecular Components in Functional Macroscopic Systems', by the German Research Foundation (DFG) within the cluster of excellence 'Center for Advancing Electronics Dresden' (cfaed, EXC1056) and by the DFG research unit 1713 'Sensoric Micro and Nanosystems'. The authors want to thank S. E. Schulz and M. Claus for collaboration and constructive discussions.

References

1. G. Overney, W. Zhong, D. Tom﹟nek, Z Phys D - Atoms, Molecules and Clusters **27**, 93 (1993)
2. M.M.J. Treacy, T.W. Ebbesen, J.M. Gibson, Nature **381**, 678 (1996)
3. Yu, Files, Arepalli, Ruoff, Physical review letters **84**, 5552 (2000)
4. J. Cao, Q. Wang, H. Dai, Physical review letters **90**, 157601 (2003)
5. R.J. Grow, Q. Wang, J. Cao, D. Wang, H. Dai, Appl. Phys. Lett. **86**, 93104 (2005)
6. C. Stampfer, A. Jungen, R. Linderman, D. Obergfell, S. Roth, C. Hierold, Nano letters **6**, 1449 (2006)
7. T. Helbling, S. Drittenbass, L. Durrer, C. Roman, C. Hierold, *Ultra Small Single Walled Carbon Nanotube Pressure Sensors: MEMS 2009 ; 25 - 29 Jan. 2009, Sorrento, Italy ; technical digest: MEMS 2009 ; 25 - 29 Jan. 2009, Sorrento, Italy ; technical digest* (IEEE, Piscataway, NJ, 2009)
8. T. Helbling, C. Roman, L. Durrer, C. Stampfer, C. Hierold, IEEE Trans. Electron Devices **58**, 4053 (2011)
9. C. Stampfer, T. Helbling, D. Obergfell, B. Schöberle, M.K. Tripp, A. Jungen, S. Roth, V.M. Bright, C. Hierold, Nano letters **6**, 233 (2006)
10. M. Muoth, K. Chikkadi, Y. Liu, C. Hierold, *Suspended CNT-FET piezoresistive strain gauges: Chirality assignment and quantitative analysis: 20 - 24 Jan. 2013, Taipei, Taiwan ; technical digest: 20 - 24 Jan. 2013, Taipei, Taiwan ; technical digest* (IEEE, Piscataway, NJ, 2013)
11. C. Wagner, J. Schuster, T. Gessner, J Comput Electron **15**, 881 (2016)
12. S. Böttger, S. Hermann, S.E. Schulz, T. Gessner, Nanotechnology **27**, 435203 (2016)
13. F. Hennrich, W. Li, R. Fischer, S. Lebedkin, R. Krupke, M.M. Kappes, ACS nano **10**, 1888 (2016)
14. Y. Kuwahara, F. Nihey, S. Ohmori, T. Saito, Carbon **91**, 370 (2015)
15. K.S. Mistry, B.A. Larsen, J.L. Blackburn, ACS nano **7**, 2231 (2013)
16. M.J. Shea, R.D. Mehlenbacher, M.T. Zanni, M.S. Arnold, The journal of physical chemistry letters **5**, 3742 (2014)
17. S.P. Schiessl, N. Fröhlich, M. Held, F. Gannott, M. Schweiger, M. Forster, U. Scherf, J. Zaumseil, ACS applied materials & interfaces **7**, 682 (2015)
18. H. Liu, D. Nishide, T. Tanaka, H. Kataura, Nature communications **2**, 309 (2011)
19. A. Vijayaraghavan, S. Blatt, D. Weissenberger, M. Oron-Carl, F. Hennrich, D. Gerthsen, H. Hahn, R. Krupke, Nano letters **7**, 1556 (2007)
20. B.K. Sarker, S. Shekhar, S.I. Khondaker, ACS nano **5**, 6297 (2011)
21. S.M. Sze, *Physics of semiconductor devices* (Wiley, New York u.a., 1996 ca)
22. A. Chaudhry, M.J. Kumar, IEEE Trans. Device Mater. Relib. **4**, 99 (2004)
23. A. Naderi, S.M. Noorbakhsh, H. Elahipanah, Journal of Nanomaterials **2012**, 1 (2012)
24. G. Fiori, G. Iannaccone, G. Klimeck, IEEE Trans. Electron Devices **53**, 1782 (2006)
25. A.K. Singh, B.N. Kumar, C.M.R. Prabhu, ECS J. Solid State Sci. Technol. **4**, M69-M72 (2015)
26. L. Ding, Z. Wang, T. Pei, Z. Zhang, S. Wang, H. Xu, F. Peng, Y. Li, L.-M. Peng, ACS nano **5**, 2512 (2011)
27. S. Böttger, S.E. Schulz, S. Hermann, Procedia Engineering **168**, 692 (2016)
28. NanoIntegris, *Technical Specifications Sheet*, http://www.nanointegris.com/en/semi-conducting
29. V. Derycke, R. Martel, J. Appenzeller, P. Avouris, Appl. Phys. Lett. **80**, 2773 (2002)
30. J. Knoch, J. Appenzeller, phys. stat. sol. (a) **205**, 679 (2008)
31. J. Luo, L. Wei, C.-S. Lee, A.D. Franklin, X. Guan, E. Pop, D.A. Antoniadis, H.-S.P. Wong, IEEE Trans. Electron Devices **60**, 1834 (2013)
32. C. Maneux, S. Fregonese, T. Zimmer, S. Retailleau, H.N. Nguyen, D. Querlioz, A. Bournel, P. Dollfus, F. Triozon, Y.M. Niquet, S. Roche, Solid-State Electronics **89**, 26 (2013)
33. I. Bejenari, M. Schroter, M. Claus, IEEE Trans. Electron Devices **64**, 3904 (2017)

34. A. Pacheco-Sanchez, M. Claus, Appl. Phys. Lett. **111**, 163108 (2017)
35. R.H. Fowler, L. Nordheim, Proceedings of the Royal Society A: Mathematical, Physical and Engineering Sciences **119**, 173 (1928)
36. Yang, Han, Physical review letters **85**, 154 (2000)
37. C.F. Wagner, *Mechanical, electronic and optical properties of strained carbon nanotubes* (Universitätsverlag Chemnitz, Chemnitz, 2017)
38. A. Kleiner, S. Eggert, Phys. Rev. B **63**, 5604 (2001)
39. F. Bogár, J.W. Mintmire, F. Bartha, T. Mező, C. van Alsenoy, Phys. Rev. B **72**, 1 (2005)
40. B.-W. Jeong, S.B. Sinnott, in *Trends in Computational Nanomechanics*, ed. by T. Dumitrica (Springer Netherlands Dordrecht, 2010), p. 255
41. C. Wagner, J. Schuster, T. Gessner, Phys. Status Solidi B **249**, 2450 (2012)
42. H. Yorikawa, S. Muramatsu, Phys. Rev. B **52**, 2723 (1995)
43. J.W. Mintmire, C.T. White, Phys. Rev. Lett. **81**, 2506 (1998)
44. C. Qiu, Z. Zhang, M. Xiao, Y. Yang, D. Zhong, L.-M. Peng, Science (New York, N.Y.) **355**, 271 (2017)
45. T. Otto, M. Messe Frankfurt GmbH (eds), *Smart Systems Integration 2018: International Conference and Exhibition on Integration Issues of Miniaturized Systems* (Wissenschaftliche Scripten, Auerbach /Vogtl., 2018)
46. W. Kim, A. Javey, O. Vermesh, Q. Wang, Y. Li, H. Dai, Nano Lett. **3**, 193 (2003)
47. T. Mizutani, S. Iwatsuki, Y. Ohno, S. Kishimoto, Jpn. J. Appl. Phys. **44**, 1599 (2005)
48. M. Hartmann, R. Schubel, M. Claus, R. Jordan, S.E. Schulz, S. Hermann, Nanotechnology **29**, 35203 (2018)
49. D. Kang, N. Park, J.-h. Ko, E. Bae, W. Park, Nanotechnology **16**, 1048 (2005)
50. P.G. Collins, Science **287**, 1801 (2000)
51. T. Helbling, C. Roman, C. Hierold, Nano letters **10**, 3350 (2010)
52. M.A. Cullinan, M.L. Culpepper, Phys. Rev. B **82** (2010)